We are IntechOpen, the world's leading publisher of Open Access books Built by scientists, for scientists

4,800
Open access books available

122,000
International authors and editors

135M
Downloads

Our authors are among the

154
Countries delivered to

TOP 1%
most cited scientists

12.2%
Contributors from top 500 universities

WEB OF SCIENCE™

Selection of our books indexed in the Book Citation Index in Web of Science™ Core Collection (BKCI)

Interested in publishing with us?
Contact book.department@intechopen.com

Numbers displayed above are based on latest data collected.
For more information visit www.intechopen.com

7

Convex Set Approaches for Material Quantification in Hyperspectral Imagery

Juan C. Valdiviezo-N and Gonzalo Urcid
Optics Department, INAOE
Mexico

1. Introduction

Emerging as the combination of optics and spectroscopy, the development of high resolution imaging spectrometers has allowed a new perspective for the monitoring, identification and quantification of natural resources in Earth's surface, that is known today as *hyperspectral remote sensing*. An imaging spectrometer is an instrument that images the energy reflected or scattered by an object in hundred of spectral bands at different portions of the electromagnetic spectrum. Although these devices have been developed for remote sensing purposes, their applications have substantially increased in the last years because of their capabilities in materials identification, being also used in biology, medicine and related areas (Huebshman et al, 2005). In contrast to multispectral devices where each imaged spectral band covers a wide spectral range, a hyperspectral sensor has a higher spectral resolution that usually is less than 10 nm; thus, the number of spectral bands captured by the sensors represents an important difference between both technologies. Once the hyperspectral data have been appropriately calibrated taking into account the illumination factors and the atmospheric effects, the spectral information registered at each pixel of the image allows a direct identification of any imaged object based on its spectrum.

When Earth observation is the application, a hyperspectral sensor usually presents a low spatial resolution caused by either the characteristics of the instrument or the flight altitude of the aerial platform, which causes that the spatial resolution decreases as the distance from the Earth increases. Considering such a sensor having a spatial resolution in the order of meters, the spectral reflectance captured in a single pixel of the image would be comprised by the mixed reflectance spectra of different materials or objects present in that physical area. Therefore, the image data will be formed by a number of pixels whose spectral information corresponds to the mixture of the constituent materials spectra. Many authors in the literature have proposed to represent these spectral mixtures as a linear combination of constituent materials spectra with their corresponding abundances (Boardman, 1993; Keshava, 2003; Winter, 1999). This model, frequently known as the *constrained linear mixing model* (CLMM), has been the basis for some autonomous techniques oriented toward the unsupervised identification of constituent materials from hyperspectral imagery, and can be considered as a convex set representation.

This chapter presents a general overview of the techniques based on a convex set representation that have been used to identify the constituent materials from a hyperspectral

scene. Besides the presentation of some classical methods used for this purpose, we are going to emphasize a recently published technique whose properties are based on lattice algebra to approximate a minimum convex set. The organization of this chapter is as follows. In Section 2 the physical foundations concerning the hyperspectral imaging process, including data characteristics and their appropriate calibration will be presented. In Section 3 we will state the necessary mathematical background to understand fundamental concepts such as minimum convex sets, affine independence, and their relation with constituent materials in hyperspectral data. Section 4 will describe some classical as well as recent techniques to achieve the autonomous endmember determination process. Section 5 will start with a brief mathematical background on lattice algebra that is necessary to understand the endmember determination method that will be described later. The section will be complemented with the presentation of two canonical lattice associative memories whose geometrical properties are used to define a convex hull from hyperspectral data. In Section 6 we will provide two application examples to illustrate the autonomous identification of natural resources from two scenes registered, respectively, over the Gulf of Mexico, and the Belstville area in Maryland (USA). Thus, the endmember identification will be realized using lattice associative memories and another novel method known as *vertex component analysis* (VCA). Finally, in section 6 we will give some pertinent comments and conclusions of this chapter.

2. Hyperspectral imaging

The development of more sophisticated imaging technologies in combination with high resolution spectrometers has given place to a new perspective in remote sensing, in which it is possible to register simultaneously the spatial and spectral information of the energy reflected from Earth's surface. These instruments, known as imaging spectrometer systems, image the Sun radiance reflected from or emitted by materials on the surface, in hundred of narrow and contiguous spectral bands usually in the reflective solar portion of the spectrum (from 0.35 to 2.5 μm). In remote sensing terminology, the region from approximately 0.35 to 1.0 μm is known as the *visible/near infrared* (VNIR) and the range from 1.0 to 2.5 μm is known as the *short wavelength infrared* (SWIR). Therefore, the resulting hyperspectral data consist of an image cube conformed by a number of radiance images that can be used to estimate the reflectance spectra of the scene. Thus, the information contained in a single pixel of a hyperspectral image can be used to compare and identify any object based on its characteristic spectrum, at a specific location of the zone of interest.

2.1 Physical foundations

There are fundamental matter-energy interaction processes that constitute the basis of the information captured by spectrometer instruments. The electromagnetic radiation coming from the sun can be modified in its direction, intensity or polarization when reaching the Earth's surface. These radiation changes depend on the physical and chemical constitution of the materials comprising the surface, and can be classified as radiation *transmission*, *reflection*, *absorption* or *emission*. When an electromagnetic wave propagating in free space reaches the frontier of a different medium, one part of its energy can be transmitted through the material and the other part can be reflected by the surface. Thus, the portion of energy that has been transmitted can be absorbed by some molecules at certain frequencies, causing an increment of the energy in their electrons and a change in the energy level. After a short time in the excitation state, the electrons return to their original state producing an emission

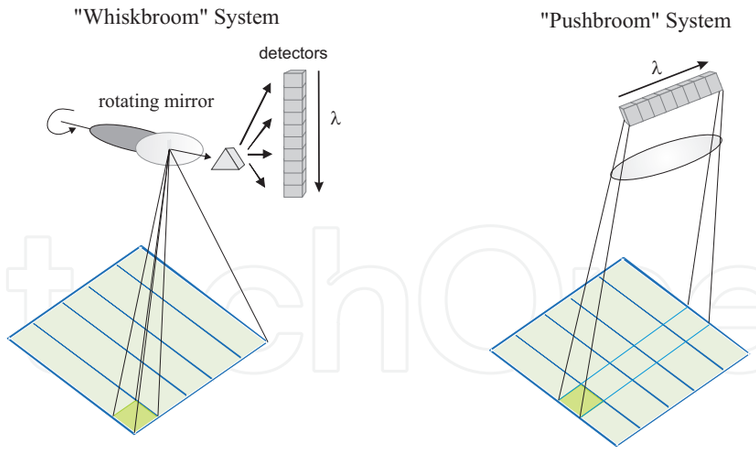

Fig. 1. Two types of scanning systems used to register a hyperspectral scene; the number of spectral bands are determined by the detectors that cover specific wavelength intervals λ.

of energy at lower frequencies. These interaction processes are used in spectroscopy for the characterization of materials in nature since they absorb or emit electromagnetic radiation at different wavelengths depending on their physical constitution. Hence, the materials covering the Earth's surface can be identified in hyperspectral data according to some absorption or emission bands present in the spectra recorded by the sensor.

For remote sensing purposes imaging spectrometers are placed onboard aerial platforms, mainly satellites or airplanes. Thus, the fundamental parts conforming hyperspectral remote sensing systems are: (1) optics to collect light, (2) a mechanism to scan the *instantaneous field of view* (IFOV) of the spectrometer over a scene, and (3) a set of spectrometers. The image acquisition process is as follows. A scanning mirror coupled to the mechanical system and the platform motion are used as part of the scanning process to collect the reflected energy coming from the surface. Furthermore, the scanning process of each line of the image can be realized using different systems. If the optics forms an image of a single point on the ground such that a line scanner scans a long line that is cross tracked to the platform motion, the scanner is called a "whiskbroom system". If the optics forms the image of a large slit such that no scan mechanism is needed other than the platform motion to form an image, the scanner is called a "pushbroom system" (see Fig. 1). Still another kind of systems use a linear variable filter over a two dimensional array of photodetectors (Jensen, 2007). After the collection of energy has been realized, the incoming light is then leaded through a set of spectrometers that splits the light into many narrow bands of energy by means of a dispersive element that can be either a grating or a prism. The energy coming from the dispersive elements is recorded by photodetectors whose sensibility responds to a specific wavelength interval, giving place to several image spectral bands.

2.1.1 Spatial and spectral resolution

In imaging spectrometers there are two basic characteristics that define the degree of resolution of the system. The *spatial resolution* is a measure of the minimum detail on the surface that can be captured for a given remote sensor. Thus, spatial resolution depends on the proper characteristics of the sensor and the flight altitude of the aerial platform. In particular, for a grating spectrograph hyperspectral imager, the spatial resolution is set by the size of the

pixels of the *charge couple device* (CCD) camera in the y direction and the microscope system magnification. However, in the x direction, the resolution depends on the spectrometer slit width and the microscope system magnification (Huebshman et al, 2005). Let Δx and Δy be respectively the x and y dimensions of the CCD pixels and the magnification be M. Note that the slit width of the spectrometer w_s is always going to be larger than Δx. Then, the spatial resolution in the y direction is $2\Delta y/M$, while in the x direction is $2w_s/M$. Moreover, other common definition of spatial resolution relating the pixel size and the flight altitude refers to the physical area over the surface occupied by a single pixel. Clearly, the resolution increases as the altitude of the aerial platform decreases.

On the other hand, the *spectral resolution* refers to the number and bandwidth of spectral bands that a sensor can register. In fact, spectral resolution depends on spectrometer components which includes the slit width, the dispersion of the grating or prism, and the sensor device pixel size. For example, for a CCD pixel size of 10 square microns, the dispersion at normal operation is determined to be approximately 40 nm per mm or, equivalently, 0.4 nm per pixel.

2.2 Reflectance estimation from sensors

The light intercepted by the entrance aperture of a sensor is the quantity know as radiance. Given that the spectral reflectance is a physical quantity that is related to material properties, it is necessary to estimate the reflectance spectra[1] from radiance information captured in hyperspectral data. For this purpose, the background energy level of the Sun must be removed and the scattering and absorbing effects of the atmosphere must be compensated for. There are three main techniques that can be used in order to estimate the spectral reflectance, which can be considered as being either an image, empirical, or model based approach. An image based approach uses only data measured by the instrument, requiring that the images include regions of relatively uniform reflectance. Thus, any absorption presented in the measured reflectance of these regions will be related with one of the mentioned effects and therefore, such effects can be compensated for the complete image. Dividing each image spectrum by the flat field spectrum, the scene is converted to relative reflectance. On the other hand, empirical methods employ both remotely sensed data and field measurements of reflectance, denoted by $r(\lambda)$, to solve a linear equation of at-sensor radiance, such that,

$$L(\lambda) = br(\lambda) + c\,, \tag{1}$$

where $L(\lambda)$ is the radiance captured by the sensor that varies with wavelength λ, and b, c represent, respectively, multiplicative and additive terms that adjust the sensor radiance.

Model based approaches seek to represent all factors involved in the radiance acquired at a pixel by pixel basis including atmospheric perturbations. For this purpose, a simulated solar irradiance spectrum is used, then the method estimates the solar radiance in the day and hour of image acquisition and the absorption and scattering effects of the atmosphere. Hence, the solar radiance impinging on sensor L_s as a function of wavelength λ can be modeled as

$$L_s(\lambda) = \frac{1}{\pi}(Er(\lambda) + M_T)\tau_\theta + L_p\,, \tag{2}$$

[1] Recall that reflectance is defined as the ratio of the energy reflected from a material to the incident light falling on it.

where E is the irradiance on the Earth's surface, $r(\lambda)$ is the reflectance of the surface, M_T is the spectral radiant exitance at temperature T, τ_θ is the transmissivity of the atmosphere at zenith angle θ and L_p is the spectral path radiance of the atmosphere (Farrand, 2005). Solving Eq. (2) gives accurate results in reflectance estimation since it includes all factors contributing to the image acquisition process. Model based approaches are also employed to estimate atmospheric properties directly from the hyperspectral data.

2.3 Imaging spectrometers

One of the first hyperspectral instruments placed onboard an aircraft for Earth observation is the *Airborne, Visible and Infrared Imaging Spectrometer* (AVIRIS). The sensor was developed at NASA's Jet Propulsion Laboratory and it is composed by a whiskbroom scanning mirror and a linear array of 224 silicon and indium-antimonide sensors. The fine spectral resolution of the instrument, around 10 nm, allows to acquire 224 spectral bands in the spectral range from 0.4 to 2.5 μm. When the sensor is placed onboard the ER-2 aircraft, flying at an altitude of 20 km above ground level, the spatial resolution of the sensor is around 400 m^2, having a 30° total field of view, and an IFOV of 1.0 mrad. However, if the instrument is placed on an aircraft flying at an altitude of 4 km over the sea level, the spatial resolution of the sensor is about 16 m^2.

Furthermore, CHRIS is a current European imaging spectrometer that is operating in its ninth year. The instrument has a spatial resolution of 17 m in up to 62 bands. The data captured by the sensor is serving in more than 50 countries to support a wide range of applications, such as, land surface and coastal zone monitoring. Other imaging spectrometers that are in use today are the *hyperspectral digital imagery collection experiment* (HYDICE) and the image spectrometers belonging to SpecTir (SpecTir, 2009).

Besides the current hyperspectral sensors, three missions are planned to work within the next five years. Italy's ASI space agency plans to launch a medium resolution hyperspectral imaging mission, known as Prisma, in 2012. The instrument will combine a hyperspectral sensor with a panchromatic medium resolution camera, being able to acquire 235 spectral bands in the VNIR and SWIR. The German Aerospace Center (DLR) and the German Research Centre for Geosciences (GFZ) are planning to launch the EnMAP hyperspectral satellite in 2014; the sensor is designed to register Earth's surface in over 200 narrow color bands at the same time. In 2015, NASA plans to launch the *Hyperspectral Infrared Imager*, known as HyspIRI. The HyspIRI mission includes two instruments mounted on a satellite in Low Earth Orbit. The first, an imaging spectrometer, will measure from the visible to short wavelength infrared at a resolution of 10 nm. Also, a multispectral sensor will cover from 3 to 12 μm in the mid and thermal infrared. Both instruments have a spatial resolution of 60 m at nadir. Thus, HyspIRI will acquire 210 spectral bands, whose data will be used to study the world's ecosystems and provide critical information on natural disasters, such as, the processes that indicate volcanic eruption, the nutrients and water status of vegetation, deforestation, among others (Esa, 2010).

3. Mathematical background

In this section, a general mathematical background is given for several endmember search techniques briefly described in the next section. Many of these techniques developed and used for the unsupervised classification of materials in hyperspectral data have been based on convex sets theory; hence, it is necessary to define some important concepts such as

minimum convex sets and endmembers together with its geometrical representation in multidimensional spaces. In the following definitions, we assume that a finite set X of n-dimensional vectors with real entries is given. Thus, using column notation we can denote this set as $X = \{\mathbf{x}^1, \ldots, \mathbf{x}^k\} \in \mathbb{R}^n$ where k is the number of vectors.

3.1 Convex sets and affine independence

In the theory of convex sets, a set of vectors $X = \{\mathbf{x}^1, \ldots, \mathbf{x}^k\} \subset \mathbb{R}^n$, also considered as points, is said to be *convex* if a straight line joining any two points resides within the set X (Lay, 2007). Being $\{a_\xi\} \subset \mathbb{R}$ a set of scalars for all $\xi \in K = \{1, \ldots, k\}$, a *linear combination* of vectors in X is an expression of the form $\sum_{\xi=1}^{k} a_\xi \mathbf{x}^\xi$. Then, X is said to be a linearly independent set if the unique solution to the equation $\sum_{\xi=1}^{k} a_\xi \mathbf{x}^\xi = \mathbf{0}$ is given by $a_\xi = 0$ for $\xi \in K$. Otherwise, the vectors in X are said to be linearly dependent. Furthermore, from a geometrical point of view, an *affine combination* is a linear combination of X subject to the condition $\sum_{\xi=1}^{k} a_\xi = 1$. If, in addition to the preceding condition, we require that $a_\xi \geq 0 \; \forall \xi \in K$ then the set is called a *convex combination* of vectors. The set of all convex combinations formed with elements of X is known as the *convex hull* of X, denoted as $C(X)$.

The notion of affine independence is of fundamental importance in the theory of convex sets and is defined as follows. Let $K_\eta = K \setminus \{\eta\}$ denote the index set from which index η has been deleted. If the set of vector differences, $X' = \{\mathbf{x}^\xi - \mathbf{x}_\eta : \xi \in K_\eta\}$ is linearly independent for some $\eta \in K$, it can be shown that X' is a linearly independent set $\forall \eta \in K$. Therefore, the set $X = \{\mathbf{x}^1, \ldots, \mathbf{x}^k\} \subset \mathbb{R}^n$ is said to be *affine independent* if and only if the set $X' = \{\mathbf{x}^\xi - \mathbf{x}_\eta : \xi \in K_\eta\} \subset \mathbb{R}^n$ is a linearly independent set for some $\eta \in K$ (Gallier, 2001). Notice that the vectors $\mathbf{x}^1, \ldots, \mathbf{x}^k$ are *affinely independent* if the unique solution to the simultaneous equations $\sum_{\xi=1}^{k} a_\xi \mathbf{x}^\xi = \mathbf{0}$ and $\sum_{\xi=1}^{k} a_\xi = 0$ is given by $a_\xi = 0$ for all $\xi \in K$. Hence, linear independence implies affine independence. It follows from this definition that any two distinct points are affinely independent, any three non-collinear points are affinely independent, and in general any m points in $\mathbb{R}^n$, with $m \leq n + 1$ are affinely independent if and only if they are not points of a common $(m-2)$-dimensional linear subspace of $\mathbb{R}^n$. The convex hull of affinely independent points form a simplex that is the minimum convex set formed by $n + 1$ vertices. In particular, if X is affinely independent, then $C(X)$ is an m-dimensional simplex or m-simplex. Thus, a 0-simplex is simply a point, a 1-simplex is a line segment determined by two affinely independent points, a 2-simplex is a triangle determined by three affinely independent points, while a 3-simplex is a tetrahedron defined by four affinely independent points.

3.2 The constrained linear mixing model

As discussed in the previous section, a noticeable characteristic of hyperspectral images is that most of the pixels contain mixtures of the spectra of constituent materials in the scene. According to the physical interaction of light with matter, it is possible to represent such mixtures using a non-linear model if we consider that photons contribute with each molecule separately. However, in this representation the estimation of the proportions of each constituent material could be a difficult task. A more practical representation, known as the *constrained linear mixing model* (CLMM), has been used to represent the spectral mixtures at a pixel basis in hyperspectral data; the CLMM model has shown to be a good approximation for

the abundance estimation of constituent materials when dealing with spectral mixtures, and it is mathematically expressed by,

$$\mathbf{x} = \sum_{i=1}^{p} a_i \mathbf{s}^i + \mathbf{r} = S\mathbf{a} + \mathbf{r} \tag{3}$$

$$a_i \geq 0 \; \forall i \quad \text{and} \quad \sum_{i=1}^{p} a_i = 1\,, \tag{4}$$

where $\mathbf{x} \in \mathbb{R}^n$ is a spectral pixel acquired over n bands, $S = \{\mathbf{s}^1, \mathbf{s}^2, \ldots, \mathbf{s}^p\}$ is an $n \times p$ matrix whose columns are the spectra of constituent materials (also known as endmembers), $\mathbf{a}=(a_1, a_2, \ldots, a_p)^t$ is a p-dimensional vector of corresponding fractional abundances present in $\mathbf{x}$ and $\mathbf{r}$ is a noise vector (Keshava, 2003). The CLMM requires the set S of p endmembers be linearly independent and, in general, that the number of endmembers be much less than the dimensionality of the data pixel spectra ($p \ll n$).

In a geometrical representation, the CLMM described above can also be thought as a minimum convex set enclosing most of the hyperspectral data, where the p pure pixels spectra are the vertices of the corresponding simplex (see Fig. 2). Moreover, because of the spatial position of pure pixels, these vertices are technically known as *endmembers*. This way, any other spectral pixel of the image belongs to this convex set and can be completely represented by those endmembers. The last statement is the cornerstone of the geometrical based approach so frequently used to extract the constituent materials spectra from hyperspectral data. Furthermore, the estimation of fractional abundances for each endmember can be performed through the inversion of Eq. (3) subject to the imposed restrictions specified by Eq. (4). This process, known as *spectral unmixing* (or *demixing*), allows to quantify the proportion of each endmember in every image pixels. A simple and direct numerical method is provided, in the unconstrained case, by the least square estimation method expressed by

$$\mathbf{a} = S^{+}\mathbf{x} = (S^t S)^{-1} S^t \mathbf{x}, \tag{5}$$

where S^{+} denotes de Moore-Penrose pseudoinverse matrix. This estimation exists when the S matrix is of full rank. The abundances that result from this estimation do not necessarily satisfy the constraints imposed in Eq.(4). Therefore, full additivity can be satisfied using the method of *Lagrange Multipliers*, while the non-negativity condition can be enforced by applying the *non-negative least squares numerical method* (Lawson & Hanson, 1974). It is also possible to employ a hybrid method in order to satisfy both constraints simultaneously.

4. Autonomous methods for endmember determination

Because the goal in the analysis of hyperspectral data is the quantification of materials comprising the scene, it is important to determine experimentally or even numerically the endmembers spectra. An experimental identification of these spectra implies the use of another device such as a spectroradiometer or a spectrometer to measure directly the reflectance spectra of materials belonging to the area under study; however this methodology is impractical in many situations because it requires an additional effort to collect samples from the zone of interest. A more practical methodology is to extract the same information as much as possible directly from the image data. In addition, assuming most pixels in the

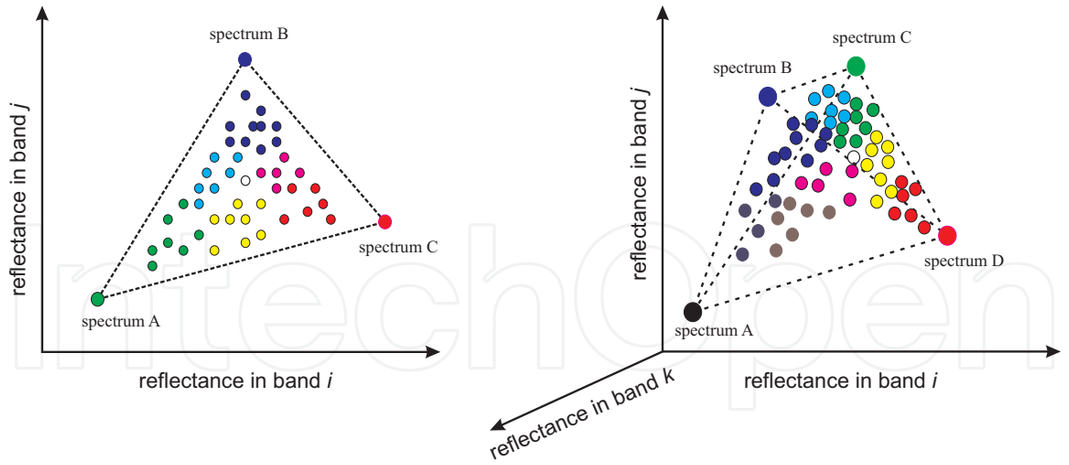

Fig. 2. Left: a 2-simplex whose vertices are three spectrally pure pixels in the image. Right: a 3-simplex defined by four spectrally pure pixels in the image defining a tetrahedron. Both simplex encloses all the spectral data.

image are conformed of spectral mixtures, then constituent materials are identified as those pixels having the spectrum of only one material. Based on this hypothesis, several authors have recently proposed and developed different methodologies used for the autonomous identification of spectrally pure pixels from the image itself. In this section we will make a review of some important techniques that have been applied for this purpose and whose methodology takes the constrained linear mixing model to represent the spectral mixtures at image pixels.

One of the earliest efforts for endmember extraction was proposed by Boardman and is known as *pixel purity index* (PPI) (Boardman, 1995). The algorithm is based on the geometry of convex sets to extract the vertices of a convex hull. Starting with a dimensionality reduction applied to the original data cube by using the minimum noise fraction transform, PPI generates a large number of random *n*-dimensional vectors, known as "skewers", through the dataset. Every pixel vector in the input data is projected onto each skewer, and its position is specified. The data that correspond to extreme points in the direction of a skewer are identified and placed on a list, indicating an increment in their pixel purity score. After many repeated projections, those pixels with a score above a certain threshold are determined as candidate "pure" pixels. From the resulting set of endmembers spectra, one can manually select those pixels that correspond to pure spectra. It is important to remark that the PPI algorithm was originally conceived as a guide to endmember determination since it requires to compare the determined spectra with those obtained from a spectral library in order to identify the final set of endmembers.

The *minimum volume transform* (MVT) algorithm, computes the minimum volume simplex enclosing the data (Craig, 1994). This proposal is based on the observation that scatter diagrams of multispectral remote sensing data tend to be triangular or pyramidal for the two or three band cases, respectively. Hence, they radiate away from the *dark-point*, which represents the sensor's response to an unilluminated object. Therefore, a minimum volume transform may be described as a non-orthogonal linear transformation of the multivariate data to new axes passing through the dark-point, and whose directions are chosen such that they embrace the data cloud. Thus, the determined MVT can be used to unmix images into new

spatial variables showing the proportions of the different cover types present in the remotely sensed scene.

The NFIND-R algorithm is an *iterative simplex volume expansion* procedure that assumes the volume contained by an n-simplex whose vertices are specified by the purest pixels is always greater than any other volume formed by other combination of pixels (Winter, 1999). The input for the algorithm is the full data cube, which after subsequent projection is reduced in dimension. The selection of these vertices is initially realized by a random selection of a set of q vectors as endmembers candidates and then computing the volume of the simplex formed by these initial endmembers. The process continues iteratively by replacing every endmember one at a time with a pixel in the image and computing the respective volume. Hence, the pixel purity likelihood is evaluated by calculating the volume for every pixel in the place of each endmember. If the replacement results in a volume increase, then the pixel replaces the corresponding endmember. The procedure is repeated until there is no more replacement of endmembers; hence, the final spectra are considered as pure pixels and can be used as endmembers to estimate their corresponding abundances. It is important to remark that the accuracy in the method depends on the initial selection of endmembers.

The algorithm termed as *vertex component analysis* (VCA), is an unsupervised technique that relies on singular value decomposition and principal component analysis as subprocedures assuming the existence of pure pixels (Nascimento & Bioucas-Dias, 2005). In particular, VCA exploits the fact that endmembers are vertices of a simplex and that the affine transformation of a simplex is also a simplex. This algorithm iteratively projects data onto a direction orthogonal to the subspace spanned by the endmembers already determined. The new endmember spectrum is the extreme of the projection and the main loop continues until all given endmembers are exhausted.

The *minimum volume enclosing symplex* (MVES) algorithm is an autonomous technique supported on a linear programming solver that does not require the existence of pure pixels in the hyperspectral data (Chan et al, 2009). For the case when there exist pure pixels, the MVES technique leads to unique identification of endmembers. In particular, dimension reduction is accomplished by affine set fitting and Craig's unmixing criterion (Craig, 1994) is applied to formulate hyperspectral unmixing as an MVES optimization problem. The algorithm first determines the affine parameters set, solves by linear programming an initial feasibility problem with linear convex constraints, and iteratively optimizes two linear programming problems with nonconvex objective functions. Notice that the algorithm requires knowing in advance the number of endmembers to be found.

5. Lattice based approach for endmember extraction

5.1 Lattice algebra operations

The use of lattice algebra for science and engineering applications in which the usual matrix operations of addition and multiplication are replaced by corresponding lattice operations, has increased in the last years. These ideas have been applied in diverse areas, such as pattern recognition (Ritter et al, 1998), associative memories in image processing (Ritter et al, 2003; Ritter & Gader, 2006; Urcid & Valdiviezo, 2009), computational intelligence (Graña, 2008), industrial applications modeling and knowledge representation (Kaburlasos & Ritter, 2007),

and hyperspectral image segmentation (Graña et al, 2009; Ritter et al, 2009; Ritter & Urcid, 2010; Valdiviezo & Urcid, 2007).

The basic numerical operations of taking the maximum or minimum of two numbers, denoted as functions $\max(x, y)$ and $\min(x, y)$, will be written as binary operators using the "join" and "meet" symbols employed in lattice theory, i.e., $x \vee y = \max(x, y)$ and $x \wedge y = \min(x, y)$. We use lattice matrix operations that are defined componentwise using the underlying structure of $\mathbb{R}_{-\infty}$ or $\mathbb{R}_{\infty}$ as semirings. For example, the maximum of two matrices X, Y of the same size $m \times n$ is defined as $(X \vee Y)_{ij} = x_{ij} \vee y_{ij}$ for $i = 1, \ldots, m$ and $j = 1, \ldots, n$. Inequalities between matrices are also verified componentwise, for example, $X \leq Y$ if and only if $x_{ij} \leq y_{ij}$. Also, the *conjugate matrix* X^* is defined as $-X^t$ where X^t denotes usual matrix transposition. Given an $m \times p$ matrix X and a $p \times n$ matix Y with entries in $\mathbb{R}$, we define a pair of dual matrix operations named as the *max-sum* and the *min-sum* denoted, respectively by $X \boxtimes Y$ and $X \boxtimes Y$ and whose i, j-th entry for $i = 1, \ldots, m$ and $j = 1, \ldots, n$, respectively, is given by $(X \boxtimes Y)_{ij} = \bigvee_{k=1}^{p} (x_{ik} + y_{kj})$ and $(X \boxtimes Y)_{ij} = \bigwedge_{k=1}^{p} (x_{ik} + y_{kj})$. For $p = 1$ these lattice matrix operations reduce to the *outer sum* of two vectors $\mathbf{x} = (x_1, \ldots, x_n)^t \in \mathbb{R}^n$ and $\mathbf{y} = (y_1, \ldots, y_m)^t \in \mathbb{R}^m$, defined by the $m \times n$ matrix

$$\mathbf{y} \times \mathbf{x}^t = \begin{pmatrix} y_1 + x_1 & \ldots & y_1 + x_n \\ \vdots & \ddots & \vdots \\ y_m + x_1 & \ldots & y_m + x_n \end{pmatrix}. \tag{6}$$

5.2 Lattice associative memories

Lattice based operations have been applied for pattern recognition problems as the computational model for a novel class of neural networks that are used as associative memories (Ritter et al, 1998). In general, let $(\mathbf{x}^1, \mathbf{y}^1), \ldots, (\mathbf{x}^k, \mathbf{y}^k)$ be k vector pairs with $\mathbf{x}^\xi = (x_1^\xi, \ldots, x_n^\xi)^t \in \mathbb{R}^n$ and $\mathbf{y}^\xi = (y_1^\xi, \ldots, y_m^\xi)^t \in \mathbb{R}^m$ for $\xi \in K$. Given a set of vector associations $\{(\mathbf{x}^\xi, \mathbf{y}^\xi) : \xi \in K\}$ we define a pair of associated matrices (X, Y), where $X = (\mathbf{x}^1, \ldots, \mathbf{x}^k)$ and $Y = (\mathbf{y}^1, \ldots, \mathbf{y}^k)$, with an association given by $(\mathbf{x}^\xi, \mathbf{y}^\xi)$ for $\xi \in K$. Thus, X is of dimension $n \times k$ with i, j-th entry x_i^j and Y is of dimension $m \times k$ with i, j-th entry y_i^j. Two $m \times n$ *lattice associative memories* able to store k vectors such that, for $\xi = 1, \ldots, k$, the memory recalls $\mathbf{y}^\xi$ when is presented the vector $\mathbf{x}^\xi$ are defined as follows: the *min-memory* W_{XY} and the *max-memory* M_{XY}, both of size $m \times n$, that store a set of associations (X, Y) are given by the expressions

$$W_{XY} = \bigwedge_{\xi=1}^{k} [\mathbf{y}^\xi \times (-\mathbf{x}^\xi)^t] \quad ; \quad w_{ij} = \bigwedge_{\xi=1}^{k} (y_i^\xi - x_j^\xi), \tag{7}$$

$$M_{XY} = \bigvee_{\xi=1}^{k} [\mathbf{y}^\xi \times (-\mathbf{x}^\xi)^t] \quad ; \quad m_{ij} = \bigvee_{\xi=1}^{k} (y_i^\xi - x_j^\xi). \tag{8}$$

The left part of Eqs. (7) and (8) are in matrix form, while the expressions to the right correspond to the i, j-th entry of *min*-W and *max*-M memories, respectively. In this case the memories are named *lattice hetero-associative* memories (LHAMs); if $X = Y$, we have a *lattice auto-associative* memory (LAAM), the case used for endmember determination. Furthermore,

the main diagonals of both memories, i.e., w_{ii} and m_{ii}, consist entirely of zeros. Since $Y = X$, $X \boxtriangledown X^* = (X^*)^* \boxtriangledown X^* = (X \boxtriangle X^*)^*$, then $M = W^*$. Hence, the *min*- and *max*-memories are dual to each other in the sense of matrix conjugation and $m_{ij} = -w_{ji}$.

5.3 Endmember determination from LAAMs

For a given set of vectors $X = \{\mathbf{x}^1, \ldots, \mathbf{x}^k\} \in \mathbb{R}^n$ and the corresponding matrix memories W_{XX} and M_{XX} computed from X, rewritten as $W = \{\mathbf{w}^1, \ldots, \mathbf{w}^n\}$ and $M = \{\mathbf{m}^1, \ldots, \mathbf{m}^n\}$ to specify their column vectors, an n-dimensional convex hull enclosing most if not all of the vectors in the given space can be derived. The points defining the convex hull will correspond to the vertices of an n-simplex and can be extracted from the columns of W and M. An important fact of the column values of LAAMs is that the relationship with the set of original data X is not direct, for example, W usually has negative values by definition. Hence, an *additive scaling* is required to relate the column values with the data set X. Thus, two scaled matrices, denoted respectively as $\overline{W}$ and $\overline{M}$, are defined for all $i = 1, \ldots, n$ according to the following expressions,

$$\overline{\mathbf{w}}^i = u_i + \mathbf{w}^i \quad ; \quad u_i = \bigvee_{\xi=1}^{k} x_i^\xi \quad ; \quad \mathbf{u} = \vee_{\xi=1}^{k} \mathbf{x}^\xi, \tag{9}$$

$$\overline{\mathbf{m}}^i = v_i + \mathbf{m}^i \quad ; \quad v_i = \bigwedge_{\xi=1}^{k} x_i^\xi \quad ; \quad \mathbf{v} = \wedge_{\xi=1}^{k} \mathbf{x}^\xi, \tag{10}$$

where $\mathbf{u}$ and $\mathbf{v}$ denotes, respectively, the *maximum* and *minimum vector bounds* of X, and whose entries are defined for all $i = 1, \ldots, n$.

Once the columns of $\overline{W}$ and $\overline{M}$ have been scaled, a fundamental result from this method is that the set of points $\overline{M} \cup \overline{W} \cup \{\mathbf{u}, \mathbf{v}\}$, forms a *convex polytope* $\mathfrak{B}$ with $2(n+1)$ vertices that contains X. These points must satisfy the affine independence condition and any subset of them can be used as endmembers. As it was proven in (Ritter & Urcid, 2010), the following theorems establish sufficient conditions to extract two subsets, W' and M' of affine independent vectors from the columns of both $\overline{W}$ and $\overline{M}$. The first theorem provides four equivalent conditions that furnish a computationally simple test for the affine independence of the sets $\overline{W}$ and $\overline{M}$; the symbols $\overline{\mathbf{w}}_i$ and $\overline{\mathbf{m}}_i$ denote the i-th row of $\overline{W}$ and $\overline{M}$, respectively; also, $\mathbf{c} = (c, \ldots, c)$ denotes a constant vector.

Theorem 1. If $i, j \in \{1, \ldots, n\}$, then the following statements are equivalent: (1) $\overline{\mathbf{w}}_i - \overline{\mathbf{w}}_j = \mathbf{c}$, (2) $\overline{\mathbf{w}}^i = \overline{\mathbf{w}}^j$, (3) $\overline{\mathbf{m}}_i - \overline{\mathbf{m}}_j = \mathbf{c}$, and (4) $\overline{\mathbf{m}}^i = \overline{\mathbf{m}}^j$.

An important consequence of the Theorem 1 is that to verify that $\overline{W}$ or $\overline{M}$ is affinely independent, all that one needs to do is to check that no two vectors of $\overline{W}$ or $\overline{M}$ are identical. The next theorem provides a simple method for deriving a set of affine independent vectors from $\overline{W}$ and $\overline{M}$. In this notation, J' denotes an arbitrary non-empty subset of J.

Theorem 2. $W' \subset \overline{W}$ is *affinely independent* if and only if $\overline{\mathbf{w}}^i \neq \overline{\mathbf{w}}^j$ for all distinct pairs $\{i, j\} \subset J'$. Similarly, $M' \subset \overline{M}$ is *affinely independent* if and only if $\overline{\mathbf{m}}^i \neq \overline{\mathbf{m}}^j$ for all distinct pairs $\{i, j\} \subset J'$.

In the next section we will use this method to derive affinely independent sets from $\overline{M} \cup \overline{W} \cup \{\mathbf{u}, \mathbf{v}\}$ as endmembers of particular data sets X.

6. Identification of endmembers: application examples

The validity in the convex set representation for endmembers identification, discussed in the previous sections, can be illustrated through experiments using real hyperspectral data sets. In fact, the aim of the application examples is to provide enough details in the use of a novel endmember determination technique. In particular, lattice auto-associative memories, W_{XX} and M_{XX}, have shown to be an efficient procedure for the autonomous endmember determination, from which a subset of final endmembers can be selected to accomplish hyperspectral image segmentation. As a complement to the theoretical results given before, the endmembers output set from the VCA algorithm will be presented and compared with that set obtained with the LAAMs method. At the end of this section, we present composite abundance maps generated from the estimation of endmember proportions using constrained linear unmixing on each hyperspectral scene.

The following data sets were taken from the SpecTir's extensive hyperspectral baseline environmental dataset (SpecTir, 2009). The available information about the image acquisition indicates that a VNIR-SWIR hyperspectral instrument, covering a wavelength range from 0.395 to 2.45 μm, was used to collect the images. Each scene has a spectral resolution of 5 nm, with a number of 360 spectral bands. Thus, a single hyperspectral cube is conformed by 600 lines $\times$ 320 pixels $\times$ 360 bands (about 132 Mbytes). Given the high spectral resolution of a hyperspectral image, a common practice to avoid redundant information consists in a spectral dimensionality reduction of the data cube by application of a chosen technique, such as principal component analysis, minimum noise fraction transform, or adjacent band removal of highly correlated bands (Keshava, 2003). These reductions are often necessary to eliminate undesirable effects produced during the acquisition process and to diminish computational requirements. Hence, in the hyperspectral cubes used for this simulation, the number of spectral bands was reduced to 90 by making a selection of spectral bands at subintervals of 20 nm covering the same wavelength interval. This spectral reduction allows to speed up the computation times with no significant effects in the endmembers identification task.

Example 1. Gulf of Mexico wetland sample

This hyperspectral cube was registered over the *Lower Suwanee National Wildlife Refuge*, which is located in the north coast of the Gulf of Mexico belonging to the USA. The Refuge lodges one of the largest undeveloped river-delta estuarine systems in this nation. Some of the numerous wildlife species that inhabit the zone are: swallow-tailed kites, bald eagles, West Indian manatees, Gulf sturgeon, whitetailed deer, and eastern wild turkeys. Natural salt marshes, tidal flats, bottomland hardwood swamps, and pine forests provide habitat for thousands of creatures. This particular hyperspectral data set was acquired at a spatial resolution of 4 m^2, covering tidal wetlands and multiple national wildlife reserves during the period of May to June 2010. In fact, the images captured the state of vegetation at the time of flights and can be used to locate the presence or absence of hydrocarbons at the surface of vegetation. Also, since the data were acquired prior to the oil disaster (occurred in 2010), they can be compared to images from later flights to assist in the damage assessments. Figure 3 shows two color composite images of the Gulf Coast hyperspectral scene. The left part of the figure

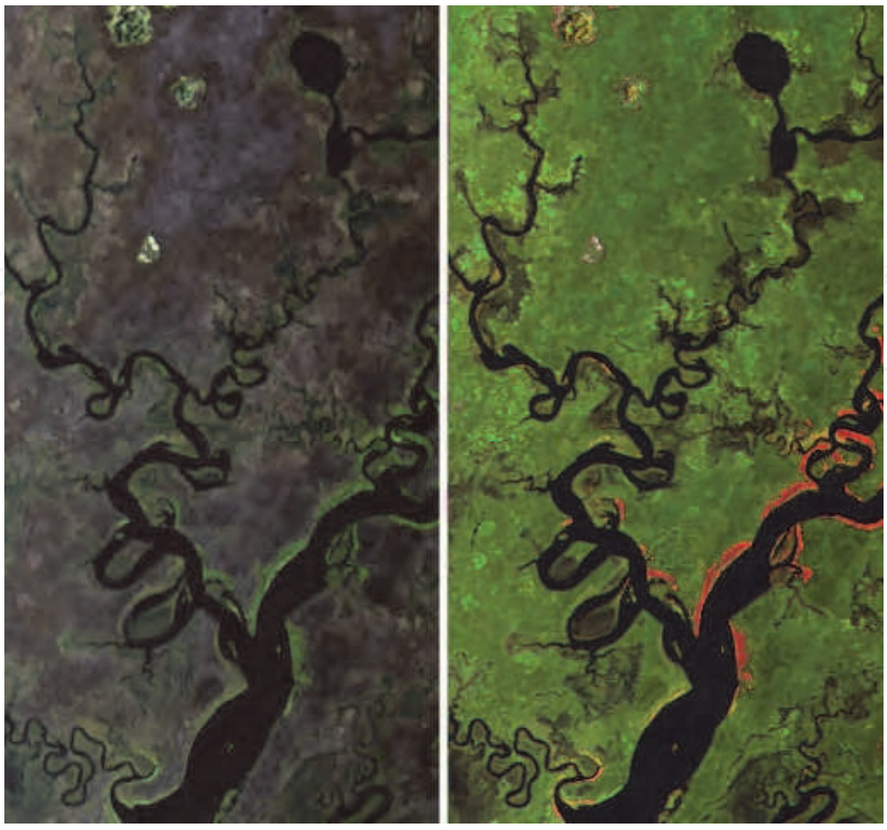

Fig. 3. Color images of the Gulf Coast hyperspectral scene used for example 1. Left: image formed by combining bands 54 (red), 34 (green) and 14 (blue). Right: combination of bands 81 (red), 217 (green), and 54 (blue).

was formed by combining bands 54 (red, λ = 693 nm), 34 (green, λ = 584 nm) and 14 (blue, λ = 469.5 nm), giving the appearance of a true color image; the right part was formed with bands 81 (red, λ = 851 nm), 217 (green, λ = 1631 nm) and 54 (blue, λ = 693 nm), whose combination using two infrared bands highlights the vegetation areas in green, orange and brown colors.

For the endmember determination process, we first form the set $X = \{\mathbf{x}^1, \ldots, \mathbf{x}^k\} \in \mathbb{R}^n$, where $k = 600 \times 320$ =192,000 and $n = 90$, arranged with the total number of spectral vectors comprising the scene. The second step consists in the computation of the memories W_{XX} and M_{XX} from X, with Eqs. (7) and (8). Using the vectors $\mathbf{v}$ and $\mathbf{u}$ calculated from Eqs. (9) and (10), the columns of W and M are then scaled to obtain $\overline{W}$ and $\overline{M}$. In order to determine a subset of affinely independent vectors, it is necessary to prove that no two columns of $\overline{W}$ or $\overline{M}$ are equal. For the application in hand, the resulting $\overline{W}$ and $\overline{M}$ are conformed, respectively by 90 affinely independent columns and, therefore, each one provides us with 90 "candidate" endmembers. In addition, because of the additive scaling previously performed, the column vectors from $\overline{W}$ present an "upward spike" since $\overline{w}_{ii} = u_i$, and vectors from $\overline{M}$ presents a "downward spike" due to $\overline{m}_{ii} = v_i$. It is then necessary to realize a simple smoothing procedure considering the

nearest one or two spectral samples next to $\overline{w}_{ii}$ or $\overline{m}_{ii}$, and is given, for any $i \in \{1, \ldots, n\}$, by

$$z_{ii} = \begin{cases} z_{1,2} & \Leftrightarrow \ i = 1, \\ \frac{1}{2}(z_{i-1,i} + z_{i+1,i}) & \Leftrightarrow \ 1 < i < n, \\ z_{n-1,n} & \Leftrightarrow \ i = n, \end{cases} \tag{11}$$

where z can be equal to $\overline{\mathbf{w}}$ or $\overline{\mathbf{m}}$. Notice that the LAAMs method always gives a number of candidate endmembers that is either equal or slightly less than the spectral dimensionality. In practice, contiguous columns are highly correlated being necessary to use some techniques to discard most of these potential endmembers. For example, minimum mutual information has been used to obtain a final set of endmembers (Graña et al, 2007); a matrix of linear correlation coefficients followed by a threshold process to get a subset of selected endmembers pairs with low correlation coefficients is introduced in (Ritter & Urcid, 2010). Here we use a simpler technique based on the fact that the LAAMs based method forms $\lfloor \sqrt{n+1} \rfloor$ subsets, each with $\lfloor \sqrt{n+1} \rfloor$ column vectors taken from W (respectively M); then, a representative from each group is selected as endmember. Although this technique provides a reasonable number of approximate true endmembers, in practical situations where a reduced number of materials comprises the hyperspectral scene, it is necessary to perform a final selection by considering those spectra that are spectrally different from the others. Therefore, in this application example, from the 20 endmembers candidates derived from $\overline{W} \cup \overline{M}$ a final selection of uncorrelated endmembers provided a reduced set containing 5 spectral vectors that forms the columns of S; thus, $S = \{\overline{\mathbf{w}}^2, \overline{\mathbf{w}}^{24}, \overline{\mathbf{w}}^{43}, \overline{\mathbf{w}}^{54}, \overline{\mathbf{w}}^{79}\}$.

On the other hand, the VCA algorithm was applied to the same hyperspectral data set. According to the implementation, the algorithm requires as input parameter the number of endmembers to be determined; the corresponding output includes the endmembers spectra as well as the pixel positions in the image from they were extracted. Repeated iterations specifying the same number of endmembers produce almost the same output set, with differences in the order in which endmembers appear. After testing different input values, such as 5, 7, 9, and 10, we decided to use the number of endmembers determined with the LAAMs method as the input parameter to the VCA algorithm. Hence, the set S of endmembers identified with VCA is conformed by $S = \{\mathbf{x}^{27876}, \mathbf{x}^{90661}, \mathbf{x}^{97850}, \mathbf{x}^{84588}, \mathbf{x}^{191634}\}$. Figure 4 displays three endmembers spectra determined from the columns selection from the set $\overline{W} \cup \overline{M}$, and whose spectral curves correspond to natural resources in the hyperspectral scene of the Gulf Coast. Similarly, Figure 5 shows three endmembers spectra obtained with application of the VCA algorithm. In both cases, normalization of reflectance data values in spectral distributions is linearly scaled from the range [0, 6000] to the unit interval [0,1]. Finally, observe that there is a similarity between spectral curves, which is indicated for curves drawn with the same colors.

Example 2. Belstville area.

The following example was performed using a hyperspectral cube registered over the Belstville area, located in northern Prince George's County in Maryland, USA. The area includes agriculture and vegetation samples. Similar to the previous image, the data cube used for this experiment is of size $600 \times 320 \times 90$, at approximately the same wavelength interval. The left part of Figure 6 displays a color composite image formed by combination of bands 54 (red, λ=693 nm), 34 (green, λ=583.9 nm), and 14 (blue, λ=469.5 nm) simulating

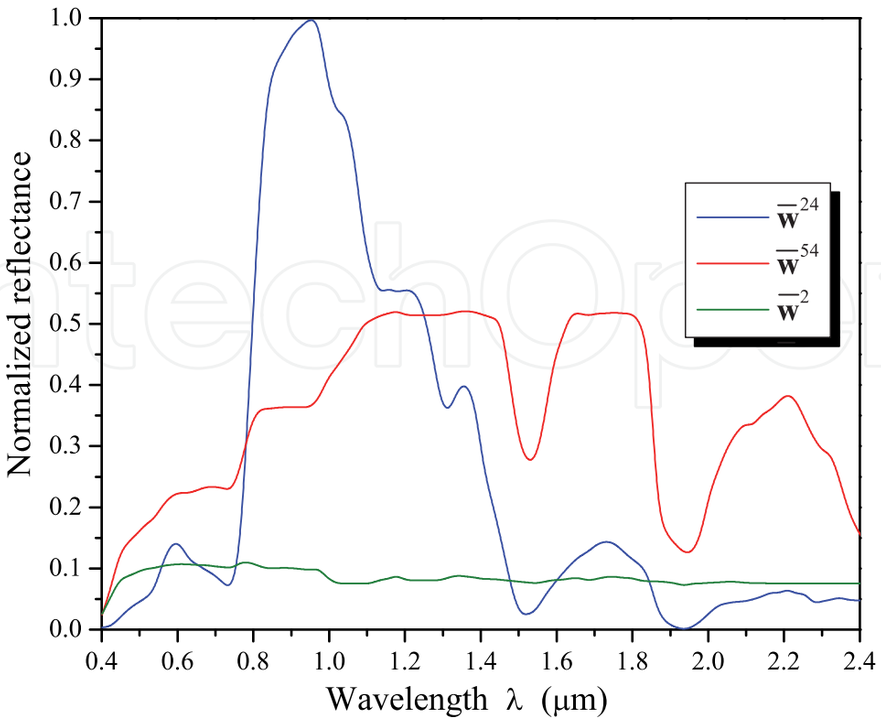

Fig. 4. Three endmembers spectra determined with application of the LAAMs method to the hyperspectral cube of the Gulf of Mexico. The associated column values selected from $\overline{W} \cup \overline{M}$ are: $\overline{\mathbf{w}}^2$, $\overline{\mathbf{w}}^{24}$, $\overline{\mathbf{w}}^{54}$.

a true color image; the right part of the same Figure shows a combination of bands 81 (red, λ=851 nm), 54 (green, λ=693 nm), and 34 (blue, λ=583.9 nm) that allows to emphasize the vegetation areas in red tones. This way, the set of all spectral vectors of the image was formed by $X = \{\mathbf{x}^1, \ldots, \mathbf{x}^k\}$, where $k = 600 \times 320 = 192,000$ and $n = 90$. Following the same procedure described in the previous example for endmember determination, we compute the memories W_{XX} and $M_{XX} = -W_{XX}^t$, as well as the vector bounds $\mathbf{u}$ and $\mathbf{v}$ used to obtain the matrices $\overline{W}$ and $\overline{M}$. Once the affine independence condition is checked, the resulting scaled memories are of size 90×90. According to the previous discussion, the spikes effects generated in the diagonal of both memories are removed using Eq. (11), and a selection of 20 endmembers candidates is made from the set $\overline{W} \cup \overline{M}$. Finally, the election of spectrally different column vectors is performed to form the final set of endmembers, whose column vectors are defined by $S = \{\overline{\mathbf{w}}^{24}, \overline{\mathbf{w}}^{37}, \overline{\mathbf{w}}^{47}, \overline{\mathbf{w}}^{64}, \overline{\mathbf{m}}^{46}, \overline{\mathbf{m}}^{57}, \overline{\mathbf{m}}^{62}\}$. Therefore, the matrix S will be used in Eq. 3 to estimate the fractional abundance of each endmember.

The VCA algorithm was applied to the set X containing all the spectral vectors of the image. As the previous example, the number of column vectors selected from the LAAMs method was established as the input parameter of the algorithm. The resulting endmembers spectra determined by VCA were used to form the matrix $S = \{\mathbf{s}^1, \ldots, \mathbf{s}^7\}$, whose spectra are associated to the column vectors $\{\mathbf{x}^{191845}, \mathbf{x}^{191419}, \mathbf{x}^{9630}, \mathbf{x}^{111446}, \mathbf{x}^{114301}, \mathbf{x}^{191724}, \mathbf{x}^{65969}\}$. Figure 7 displays four of the final endmembers set obtained with the selection of vectors from $\overline{W} \cup \overline{M}$; Figure 8 shows four of the endmembers spectra determined by the VCA algorithm that are similar to those computed with the LAAMs method. The similarity between spectral curves

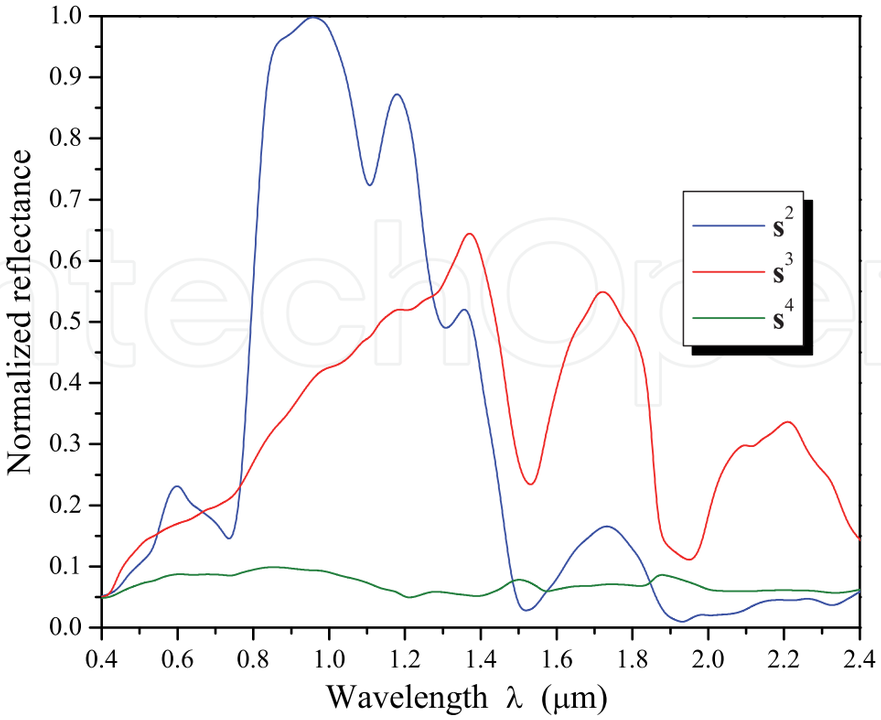

Fig. 5. Three endmembers spectra obtained with application of the VCA algorithm to the hyperspectral cube of the Gulf of Mexico. The column vectors $\mathbf{s}^j$ for $j = 1, \ldots, 5$ indicate the corresponding column of the S matrix.

can be identified for curves drawn in the same color. Although the spectral curves in both sets seem to be alike, a similarity measure must be applied in order to quantify these similarities. Here, we have computed the correlation coefficients between the sets obtained with the LAAMs method and the VCA algorithm, for each one of the application examples. Table 1 presents the correlation coefficients computed for the spectral curves displayed in Figures 4, 5 and 7, 8, respectively.

Gulf of Mexico		Beltsville	
VCA & LAAMs	Corr. Coef.	VCA & LAAMs	Corr. Coef.
$\mathbf{s}^2$ and $\overline{\mathbf{w}}^{24}$	0.980	$\mathbf{s}^1$ and $\overline{\mathbf{w}}^{37}$	0.965
$\mathbf{s}^3$ and $\overline{\mathbf{w}}^{54}$	0.974	$\mathbf{s}^2$ and $\overline{\mathbf{w}}^{24}$	0.944
$\mathbf{s}^4$ and $\overline{\mathbf{w}}^{2}$	0.641	$\mathbf{s}^3$ and $\overline{\mathbf{w}}^{64}$	0.912
–	–	$\mathbf{s}^4$ and $\overline{\mathbf{w}}^{47}$	0.939

Table 1. Correlation coefficients for similar spectra obtained with the LAAMs method and the VCA algorithm from the hyperspectral images of the Gulf of Mexico and Beltsville.

6.1 Constrained linear unmixing

The spectral unmixing process can be realized by means of the inversion expressed in Eq. (5), subject to the restrictions of full additivity and non-negativity of abundance coefficients. Notice that Eq. (3) is an *overdetermined* system of linear equations such that $n > p$. For the examples here discussed, both matrices $\overline{W}$ and $\overline{M}$ have full rank, thus their column vectors

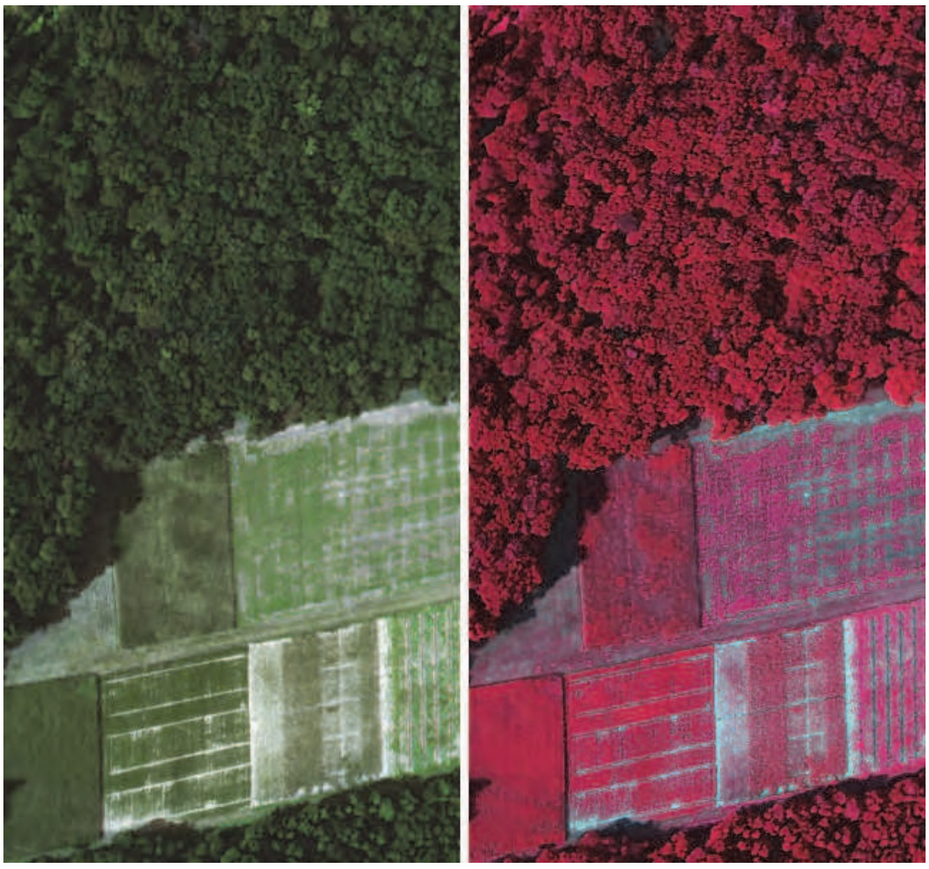

Fig. 6. Color images of Beltsville hyperspectral scene used fot example 2. Left: image formed by combining bands 54 (red), 34 (green) and 14 (blue). Right: combination of bands 81 (red), 54 (green), and 34 (blue).

are linearly independent. In addition, the set of final endmembers, either determined with the LAAMs method or those identified by the VCA algorithm, is a linear independent set whose pseudoinverse matrix is unique. Although the unconstrained solution corresponding to Eq. (5), where $n > p$ ($n = 90$ and $p = 7$ or $p = 5$), has a single solution, some coefficients may be negative for many pixel spectra and do not sum up to unity. If full additivity is enforced, negative coefficients appear. Therefore, the best approach consists of imposing non-negativity for the abundance proportions, relaxing full additivity by considering the inequality $\sum_{i=1}^{p} a_p < 1$. For the examples here presented we use the *non-negative least squares* (NNLS) algorithm that solves the problem of minimizing the Euclidian norm $\|S\mathbf{a} - \mathbf{x}\|_2$ subjected to the condition $\mathbf{a} > 0$ (Lawson & Hanson, 1974).

Figure 9 displays the color abundance maps of the endmembers determined with each one of the methods here discussed. These maps were generated using the NNLS numerical method implemented in Matlab 7.6; in these images, brighter areas represent maximum distribution of the corresponding endmember. The left part of Figure 9 shows the distribution of four natural resources that were determined with implementation of the LAAMs method in the hyperspectral cube of the Gulf Coast. The right part of the same Figure displays the distribution of three natural resources that were determined using the VCA algorithm. In

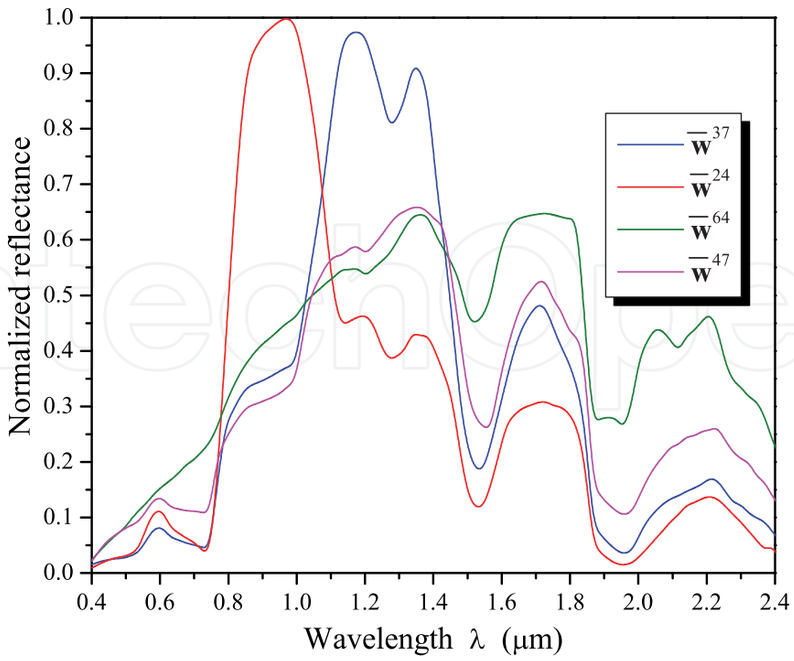

Fig. 7. Four endmembers spectra determined with application of the LAAMs method to the hyperspectral cube of Beltsville. The associated column vectors selected from $\overline{W} \cup \overline{M}$ are: $\overline{\mathbf{w}}^{24}$, $\overline{\mathbf{w}}^{37}$, $\overline{\mathbf{w}}^{47}$, $\overline{\mathbf{w}}^{64}$.

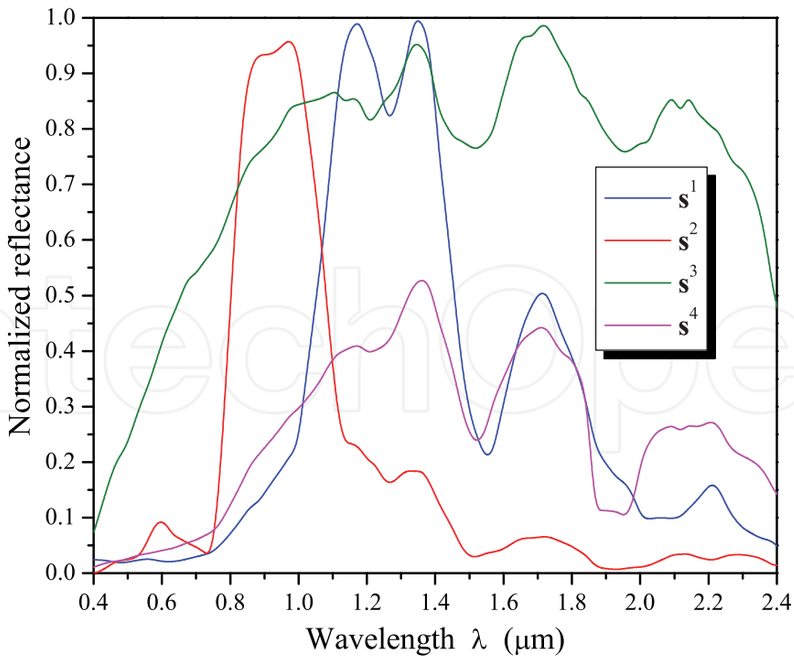

Fig. 8. Four endmembers spectra obtained with application of the VCA algorithm to the hyperspectral cube of Belstville. The column vectors $\mathbf{s}^j$ for $j = 1, \ldots, 7$ indicate the corresponding column of the S matrix.

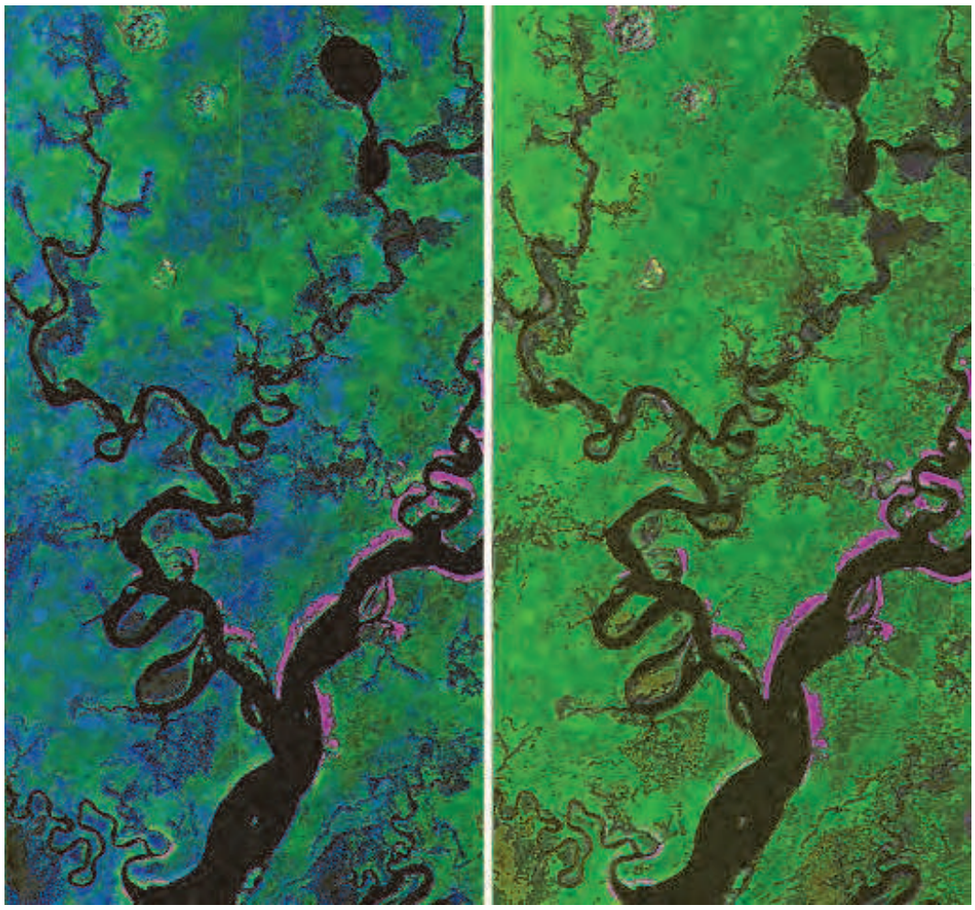

Fig. 9. Color abundance maps of natural resources determined with the autonomous identification of endmembers in the hyperspectral cube of the Gulf Coast. Left: abundances of four endmembers determined with the LAAMs method, whose distribution of colors corresponds to yellow = $\overline{\mathbf{w}}^2$, magenta = $\overline{\mathbf{w}}^{24}$, green = $\overline{\mathbf{w}}^{43}$, blue = $\overline{\mathbf{w}}^{54}$. Right: abundances of three endmembers determined with the VCA algorithm whose distribution of colors is yellow = $\mathbf{s}^4$, magenta = $\mathbf{s}^2$, green = $\mathbf{s}^3$. Brighter areas mean higher distributions of the corresponding natural resource.

both cases we present only the abundance maps that provide meaningful information; thus, the maps presenting redundant information or predominant dark areas were not included. Although the region is characterized by the presence of wetlands, it has not been possible to use a set of reference spectra to identify the natural resources. Furthermore, Figure 10 displays the color abundance maps of the endmembers determined with the LAAMs method (left part), as well as the VCA algorithm (right part) from the hyperspectral data cube of Beltsville. Although the set S has conformed by seven endmembers spectra, we have included in both cases the abundance maps that best match the distribution of vegetation according to a visual inspection of Figure 6. In this example, it is evident that the identification of vegetation types, produced with each one of the methods, presents similar results for the segmentations colored in yellow and magenta. However, the results presents important differences particularly in the green and blue segmentations. These differences are mainly caused by the endmember search procedure used in each technique; in addition, the fact that spectral curves of vegetation types

are alike, varying in certain absorption bands, contributes with the disagreements in these segmentation results.

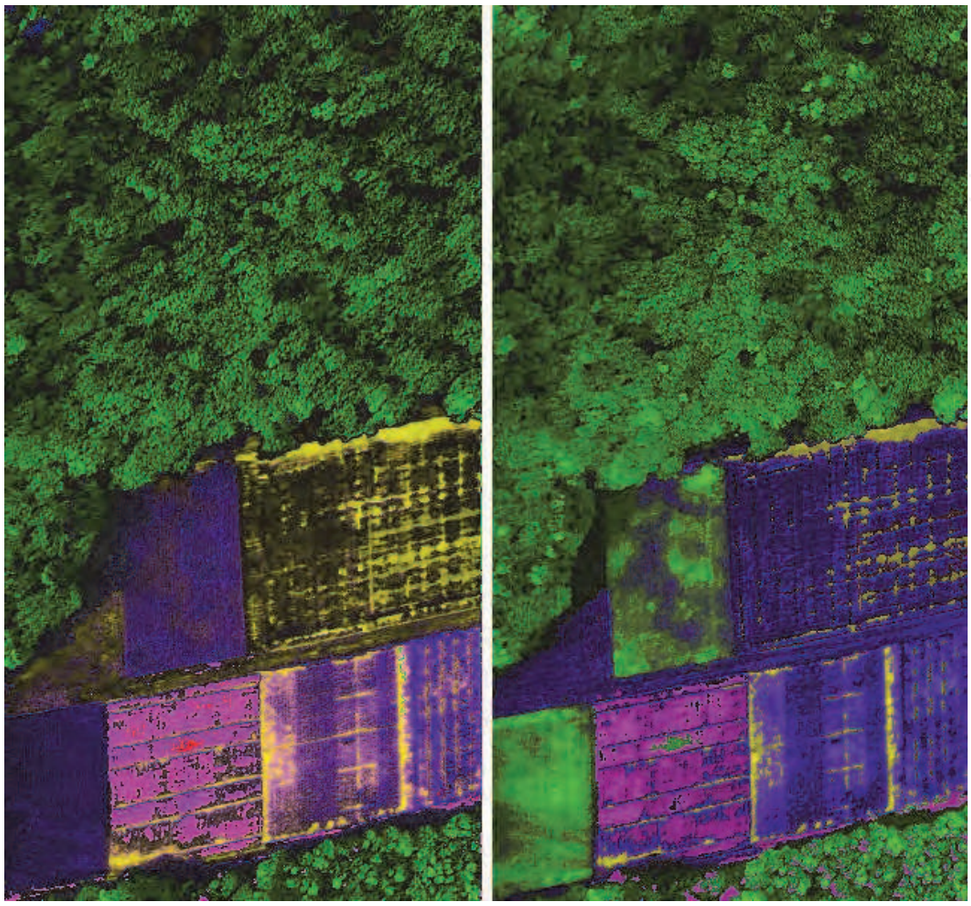

Fig. 10. Color abundance maps of vegetation types obtained with the autonomous identification of endmembers in the Belstville hyperspectral image. Left: abundances of four endmembers determined with the LAAMs method whose distribution of colors corresponds to magenta = $\overline{\mathbf{w}}^{24}$, yellow = $\overline{\mathbf{w}}^{67}$, blue = $\overline{\mathbf{m}}^{46}$, green = $\overline{\mathbf{m}}^{62}$. Right: abundances of four endmembers determined with the VCA algorithm, whose distribution of colors is magenta = $\mathbf{s}^2$, yellow = $\mathbf{s}^3$, blue = $\mathbf{s}^5$, green = $\mathbf{s}^7$. Brighter areas correspond to higher distributions of the corresponding natural resource.

7. Conclusion

The use of high resolution image spectrometers for Earth observation purposes has given place to different applications oriented toward the identification, classification and monitoring of natural resources from remotely sensed data. In this chapter we have described the physical foundations behind the acquisition and calibration of hyperspectral imagery that constitute the basis of modern hyperspectral instruments, such as AVIRIS, HYDICE, and SpecTir's imaging spectrometers. Also, we have made a review of past, as well as recent methods for the autonomous endmember determination process based on the geometry of convex sets. The mathematical foundation behind these methods is to model the spectral mixtures acquired at a pixel basis as a linear combination of constituent materials. Hence,

the aim of these techniques is to determine the constituent materials that are identified as the purest pixels in the scene. Among the methods discussed, we have emphasized a lattice algebra based method that uses two canonical associative memories, the min-W_{XX} and the max-M_{XX}, to determine a $2(n+1)$-simplex enclosing the hyperspectral data set. Thus, any subset of vertices of the simplex can be used as the endmember set to perform the unmixing process. The application of the LAAMs method and the VCA algorithm for the autonomous segmentation of real hyperspectral scenes taken from the SpecTir's imaging spectrometer has shown the effectiveness of convex set approaches. Although there exist some differences in the results obtained with both methods, any of them can be used for unsupervised hyperspectral segmentation, in particular if there is no reference data of the area, as the example cases treated in this chapter.

8. Acknowledgments

The authors acknowledge to SpecTir for providing the data sets used in these experiments. Juan C. Valdiviezo-N thanks the National Council of Science and Technology (CONACYT) for doctoral scholarship # 175027. Gonzalo Urcid is grateful with the National Research System (SNI-CONACYT) for partial financial support through grant # 22036.

9. References

Boardman J.W. (1993). Automated spectral unmixing of AVIRIS data using convex geometry concepts, *Proceedings of AVIRIS Workshop*, Vol. 4, pp. 11–14, USA, JPL Publication.

Boardman J.W. (1995). Analysis, understanding and visualization of hyperspectral data as convex sets in *n*-space, *Proceedings of SPIE, Imaging Spectrometry*, Vol. 2480, pp. 14–22, Orlando, FL, USA, April, 1995, SPIE Press.

Chan, T-H. Chi, C-Y. Huang, Y-M. and Ma, W-K. (2009). A convex analysis based minimum volume enclosing simplex algorithm for hyperspectral unmixing. *IEEE Trans. on Signal Processing*, Vol. 57, Issue 11, June 2009, pp. 4418–4432.

Craig M.D. (1994). Minimum-volume transforms for remotely sensed data, *IEEE Trans. on Geoscience and Remote Sensing*, Vol. 32, No. 3, May 1994, pp. 542–552.

Esa (2010). European Space Agency, website: www.esa.int.

Farrand W.H. (2005). Hyperspectral remote sensing of land and the atmosphere, In: *Encyclopedia of Modern Optics*, Vol. 1, Robert D. Guenther editor, pp. 395–403, Elsevier, Academic Press.

Gallier J. (2001). Geometric Methods and Applications for Computer Science and Engineering, In: *Texts in Applied Mathematics*, Vol. 38, Springer, New York.

Graña, M. Jiménez, J.L. Hernàndez, C. (2007). Lattice independence, autoassociative morphological memories and unsupervised segmentation of hyperspectral images, *Proceedings of the 10th joint Conference on Information Sciences*, NC-III, pp. 1624-1631, World Scientific Publishing Co.

Graña, M. (2008). A brief review of lattice computing, *Proceedings of IEEE, World Congress on Computational Intelligence*, pp. 1777–1781, Hong Kong, June 2008, IEEE Press.

Graña, M. Villaverde, I. Maldonado, J.O. Hernández, C. (2009). Two lattice computing approaches for the unsupervised segmentation of hyperspectral images, *Neurocomputing*, Vol. 72, No. 10-12, June 2009, pp. 2111–2120.

Huebshman M.L., Schultz R.A., Garner H.R. (2005). Hyperspectral imaging, In: *Encyclopedia of Modern Optics*, Vol. 1, Robert D. Guenther editor, pp. 134–143, Elsevier, Academic Press.

Jensen, J.R. (2007). *Remote Sensing of the Environment: an Earth Resource Perspective*, 2nd edition, Pearson Prentice Hall.

Kaburlasos, V.G. Ritter G.X. (eds.) (2007), *Computational Intelligence based on Lattice Theory*, Vol. 67. Springer Verlag, Heidelberg, Germany.

Keshava N. (2003). A survey of spectral unmixing algorithms, *Lincoln Laboratory Journal*, Vol. 14, No. 1, pp. 55–78.

Keshava, N. and Mustard, J.F. (2002). Spectral unmixing, *IEEE Signal Processing Magazine*, Vol. 19, No. 1, January 2002, pp. 44–57.

Lawson, C.L. Hanson, R.J. (1974). *Solving least squares problems*, chap. 23, Prentice-Hall, Englewood Cliffs NJ.

Lay, S.R. (2007). *Convex Sets and Their Applications,* Dover Publications, New York, USA.

More, K.A. (2005). Spectrometers, In: *Encyclopedia of Modern Optics*, Vol. 1, Robert D. Guenther editor, pp. 324–336, Elsevier, Academic Press.

Nascimento, J.M.P. and Bioucas-Dias, J.M. (2005). Vertex component analysis: a fast algorithm to unmix hyperspectral data, *IEEE Trans. on Geoscience and Remote Sensing*, Vol. 43, No. 4, April 2005, pp. 898–910.

Ritter, G.X. Sussner, P. Díaz de León, J.L. (1998). Morphological associative memories, *IEEE Trans. Neural Networks*, Vol. 9, No. 2, March 1998, pp. 281–293.

Ritter, G.X. Urcid G., and Iancu, L. (2003). Reconstruction of noisy patterns using morphological associative memories, *Journal of Mathematical Imaging and Vision*, Vol. 19, No. 5, pp. 95–111.

Ritter, G.X. Gader, P. (2006). Fixed points of lattice transforms and lattice associative memories. In: *Advances in imaging and electron physics*, Vol. 144, P. Hawkes editor, 165–242. Elsevier, San Diego, CA.

Ritter, G.X. Urcid, G. Schmalz, M.S. (2009). Autonomous single-pass endmember approximation using lattice auto-associative memories, *Neurocomputing*, Vol. 72, Issues 10-12, June 2009, pp. 2101–2110.

Ritter, G.X., Urcid G. Lattice algebra approach to endmember determination in hyperspectral imagery. In: *Advances in Imaging and Electron Physics*, Vol. 160, Peter W. Hawkes editor, pp. 113-169, Elsevier Inc, Academic Press.

SpecTir (2009). SpecTir: end to end hyperspectral solutions, website: www.spectir.com.

Urcid, G. Valdiviezo-N., J.C. (2007). Generation of lattice independent vector sets for pattern recognition applications, *SPIE Proceedings, Mathematics of Data/Image Pattern Recognition, Compression, Coding, and Encryption X with Applications*, Vol. 6700, pp. 67000C :1–12, San Diego, CA, August 2007, SPIE Press.

Urcid, G. Valdiviezo, J.C. (2009). Color image segmentation based on lattice auto-associative memories, *Proceeding of IASTED, Artificial ingelligence and soft computing*, pp. 166-173, Palma de Mallorca, Spain, September 2009, Acta Press.

Valdiviezo, J.C. and Urcid, G. (2007). Hyperspectral endmember detection based on strong lattice independence, *Proc. SPIE, Applications of Digital Image Processing XXX*, Vol. 6696, pp. 669625 :1–12, San Diego, CA, USA, August 2007, SPIE Press.

Winter M.E. (1999). NFIND-R: an algorithm for fast autonomous spectral endmember determination in hyperspectral data, *Proceedings of SPIE, Imaging Spectrometry V*, Vol. 3753, pp. 266–275, Denver, CO, USA, July 1999, SPIE Press.

Winter M.E. (2000). Comparison of approaches for determining end-members in hyperspectral data, *Proceedings of IEEE: Aerospace Conference*, Vol. 3, pp. 305–313, Big Sky, MT, USA, March 2000, IEEE Press.

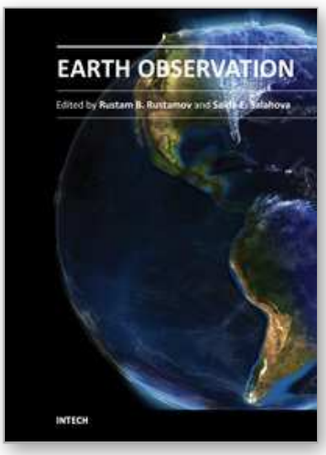

Earth Observation

Edited by Dr. Rustam Rustamov

ISBN 978-953-307-973-8
Hard cover, 254 pages
Publisher InTech
Published online 27, January, 2012
Published in print edition January, 2012

Today, space technology is used as an excellent instrument for Earth observation applications. Data is collected using satellites and other available platforms for remote sensing. Remote sensing data collection detects a wide range of electromagnetic energy which is emitting, transmitting, or reflecting from the Earth's surface. Appropriate detection systems are needed to implement further data processing. Space technology has been found to be a successful application for studying climate change, as current and past data can be dynamically compared. This book presents different aspects of climate change and discusses space technology applications.

How to reference

In order to correctly reference this scholarly work, feel free to copy and paste the following:

Juan C. Valdiviezo-N and Gonzalo Urcid (2012). Convex Set Approaches for Material Quantification in Hyperspectral Imagery, Earth Observation, Dr. Rustam Rustamov (Ed.), ISBN: 978-953-307-973-8, InTech, Available from: http://www.intechopen.com/books/earth-observation/convex-set-approaches-for-material-quantification-in-hyperspectral-imagery

INTECH
open science | open minds

InTech Europe
University Campus STeP Ri
Slavka Krautzeka 83/A
51000 Rijeka, Croatia
Phone: +385 (51) 770 447
Fax: +385 (51) 686 166
www.intechopen.com

InTech China
Unit 405, Office Block, Hotel Equatorial Shanghai
No.65, Yan An Road (West), Shanghai, 200040, China
中国上海市延安西路65号上海国际贵都大饭店办公楼405单元
Phone: +86-21-62489820
Fax: +86-21-62489821

IntechOpen